nature physics

Article

https://doi.org/10.1038/s41567-023-02348-1

Nodal $s_{\pm}$ pairing symmetry in an iron-based superconductor with only hole pockets

Received: 23 November 2022

Accepted: 23 November 2023

Published online: 23 January 2024

Check for updates

Dingsong Wu[1,2,3,7], Junjie Jia[1,2,7], Jiangang Yang[1,2,7], Wenshan Hong[1,2], Yingjie Shu[1,2], Taimin Miao[1,2], Hongtao Yan[1,2], Hongtao Rong[1,2], Ping Ai[1,2], Xing Zhang[1,2], Chaohui Yin[1,2], Jieyi Liu[3], Houke Chen[3], Yiheng Yang[3], Cheng Peng[3], Chenlong Li[4], Shenjin Zhang[4], Fengfeng Zhang[4], Feng Yang[4], Zhimin Wang[4], Nan Zong[4], Lijuan Liu[4], Rukang Li[4], Xiaoyang Wang[4], Qinjun Peng[4], Hanqing Mao[1,2,5], Guodong Liu[1,2,5], Shiliang Li[1,2,5], Yulin Chen[3], Huiqian Luo[1,2,5], Xianxin Wu[6], Zuyan Xu[4], Lin Zhao[1,2,5] ✉ & X. J. Zhou[1,2,5] ✉

The origin of high-temperature superconductivity in iron-based superconductors is still not understood; determination of the pairing symmetry is essential for understanding the superconductivity mechanism. In the iron-based superconductors that have hole pockets around the Brillouin zone centre and electron pockets around the zone corners, the pairing symmetry is generally considered to be $s_{\pm}$, which indicates a sign change in the superconducting gap between the hole and electron pockets. For the iron-based superconductors with only hole pockets, however, a couple of pairing scenarios have been proposed, but the exact symmetry is still controversial. Here we determine that the pairing symmetry in KFe_2As_2—which is a prototypical iron-based superconductor with hole pockets both around the zone centre and around the zone corners—is also of the $s_{\pm}$ type. Our laser-based angle-resolved photoemission measurements have determined the superconducting gap distribution and identified the locations of the gap nodes on all the Fermi surfaces around the zone centres and the zone corners. These results unify the pairing symmetry in hole-doped iron-based superconductors and point to spin fluctuation as the pairing glue in generating superconductivity.

Iron-based superconductors were discovered more than a decade ago, but the mechanism of their superconductivity remains an outstanding issue in condensed matter physics[1–4]. Identification of the pairing symmetry and of the medium that provides the pairing glue are two key prerequisites for understanding the superconductivity mechanism. As a typical multiorbital system, a number of pairing symmetries have been proposed in iron-based superconductors that are associated with different pairing glues[1–4]. In most iron-based superconductors with hole-like Fermi surfaces around the zone centre and electron-like Fermi surfaces around the zone corners, an $s_{\pm}$ pairing symmetry is expected from spin fluctuations based on a weak coupling Fermi surface nesting picture[5,6] or a strong coupling local magnetic picture[7,8]. In some iron-based superconductors with only electron-like Fermi surfaces[9–13], the d-wave pairing is found to be dominant from electron scatterings between the zone corners by spin fluctuations[6,14,15] and a transition from d wave to s wave with increasing band hybridization has been proposed[16]. For the

[1]Beijing National Laboratory for Condensed Matter Physics, Institute of Physics, Chinese Academy of Sciences, Beijing, China. [2]University of Chinese Academy of Sciences, Beijing, China. [3]Department of Physics, University of Oxford, Oxford, UK. [4]Technical Institute of Physics and Chemistry, Chinese Academy of Sciences, Beijing, China. [5]Songshan Lake Materials Laboratory, Dongguan, China. [6]Institute of Theoretical Physics, Chinese Academy of Sciences, Beijing, China. [7]These authors contributed equally: Dingsong Wu, Junjie Jia, Jiangang Yang. ✉e-mail: lzhao@iphy.ac.cn; xjzhou@iphy.ac.cn

iron-based superconductors with only hole-like Fermi surfaces, there is still controversy about whether the pairing is nodal or nodeless[17–25] and whether it is *d* wave or *s* wave[18–31]. Direct determination of the gap structure in purely hole-doped iron-based superconductors is important for ascertaining their pairing symmetry and establishing a unified picture of the pairing mechanism in iron-based superconductors.

As the end member of hole-doped $(Ba_{1-x}K_x)Fe_2As_2$, KFe_2As_2 is a prototypical system for studying the superconductivity mechanism in purely hole-doped iron-based superconductors. It has a unique electronic structure that consists of only hole pockets[32–34]. It has been found that KFe_2As_2 has a large Sommerfeld coefficient that behaves similarly to heavy Fermion materials[33,35–40], which indicates the presence of strong electron correlation due to its proximity to the putative Mott insulating state[41]. However, the electronic origin of its heavy-electron behaviour has not been conclusively proved. More importantly, although extensive studies have been carried out to probe the pairing symmetry of KFe_2As_2, the pairing nature has not been pinned down and remains controversial[17–21,23–25,29–31].

To determine the superconducting gap structure of KFe_2As_2 and other unconventional superconductors with low T_C (superconducting critical temperature) and small superconducting gap, we developed a laser angle-resolved photoemission spectroscopy (ARPES) system with ultra-low temperature (0.8 K) and superhigh energy resolution (less than 0.5 meV) (Methods). We also grew high-quality KFe_2As_2 single crystals with a T_C at 3.7 K and a sharp superconducting transition (0.2 K) (Methods and Supplementary Fig. 1). We resolved the complete Fermi surface topology and band structures of KFe_2As_2, in particular, those near the Brillouin zone corners, by taking advantage of surface reconstruction. We determined precisely the momentum-dependent superconducting gap on each Fermi surface and identified the locations of the gap nodes. These results unravel the electronic origin of the huge mass enhancement and strong electron correlation in KFe_2As_2. They also provide strong evidence on the $s_{\pm}$ pairing symmetry with a sign reversal between the zone centre and zone corners in the system with only hole pockets.

Figure 1 shows the measured Fermi surface and band structures of KFe_2As_2. As a typical multiorbital system, we find that strong photoemission matrix element effects are involved in the ARPES measurements of KFe_2As_2. Therefore, to fully resolve the Fermi surface and band structures, we carried out ARPES measurements using different light polarizations (Supplementary Fig. 2). Combining the Fermi surface mapping (Fig. 1a) and the associated band structures (Fig. 1c–f and Supplementary Fig. 3) measured under various polarization geometries, we obtained the complete Fermi surface picture of KFe_2As_2, as shown in Fig. 1b. It consists of three main Fermi surface sheets around Γ (α, β and γ in Fig. 1b), a small surface state sheet around Γ (SS in Fig. 1b) and four hole pockets around M (ε in Fig. 1b). The orbital characteristics of the Fermi surface were analysed and are shown in Supplementary Fig. 4 and Supplementary Tables 1–2. Our more precise measurements of the Fermi surface (Fig. 1b) indicate that it is rather similar to the Fermi surface at $k_z \approx 0$ (k_z is the momentum perpendicular to the a–b plane) from the previous three-dimensional ARPES measurements[34], which indicates that the measured momentum region is close to Γ point ($k_z \approx 0$) in our ARPES results using 7 eV photons. We find that the β Fermi surface further splits into two sheets (β_1 and β_2 in Fig. 1b) with the maximum splitting along Γ–X, as seen from the band structure in Fig. 1f. Our further synchrotron-based ARPES measurements indicate that the β_1 band is from the bulk state whereas the β_2 band can be attributed to a surface state (Supplementary Figs. 5 and 6).

Although laser ARPES is advantageous in taking high-quality data with superhigh resolution, it has a limitation in the covered momentum space due to its lower photon energy[21,42]. Particularly for the iron-based superconductors, laser ARPES can cover mainly the zone centre region but cannot reach the zone corner M points[21,42]. It is interesting and noteworthy that, in this study, we observed the Fermi surface and band structures around M that are folded to the region around Γ. Under a proper polarization geometry, four Fermi pockets were observed around Γ, which are marked by dashed pink lines and labelled as ε′ in Fig. 1a. The corresponding band structures (the left and right branches of ε′ band ε'_L and ε'_R in Fig. 1c,d) were resolved and their spectral intensity was comparable to that of the α, β and γ bands. These four ε′ pockets can be well attributed to the four ε hole pockets around M that are folded to the Γ point by the $\sqrt{2} \times \sqrt{2}$ surface reconstruction (Supplementary Figs. 7–10). Such a band folding makes it possible to study the electronic structure and superconducting gap of KFe_2As_2 in the full momentum space by laser ARPES.

Figure 2 highlights the band structures and photoemission spectra measured in the normal and superconducting states. Clear quasiparticle peaks were observed in the photoemission spectra (energy distribution curves (EDCs)) measured along all the Fermi surface sheets at 4.3 K in the normal state (red curves in left-hand panels of Fig. 2e–l). Superconducting coherence peaks developed in some EDCs in the superconducting state at 0.9 K (blue curve in left-hand panels of Fig. 2e,f,k). The observed peaks are rather sharp with a width (full-width at half-maximum) of 1–2 meV. To visualize the gap opening, band symmetrization or EDC symmetrization with respect to the Fermi level is usually carried out to remove the Fermi distribution function[43]. In this case, the gap opening corresponded to the spectral weight suppression at the Fermi level. As visualized in Fig. 2b,c, in the superconducting state at 0.9 K, the spectral weight at the Fermi level for the α, β, ε'_L and SS bands was obviously suppressed, which indicated the opening of the superconducting gap. In the symmetrized EDCs measured at 0.9 K (blue curves in the right-hand panels of Fig. 2e–l), the spectral weight suppression at the Fermi level was observed for P1 on the α band (Fig. 2e), for P2 on the β band (Fig. 2f) and for P7 on the ε'_L band (Fig. 2k), which signalled the opening of the superconducting gap (the location of the Fermi momentum points P1–P8 is shown in Fig. 2d). The gap size was determined from the energy difference between the two peaks in the symmetrized EDCs. On the other hand, the symmetrized EDCs in the superconducting state exhibited a peak at the Fermi level at other momentum points (blue curves in Fig. 2g–j,l), which indicated that no superconducting gap opening was detected within our experimental precision. In all the symmetrized EDCs measured at 4.3 K in the normal state (red curves in the right-hand panels of Fig. 2e–l), there was no signature of gap opening observed, excluding the formation of a pseudogap in KFe_2As_2.

It was found that KFe_2As_2 exhibits heavy Fermion behaviours manifested by its large Sommerfeld coefficient and heavy effective mass[33,35–39]. Our present high-resolution band structure measurements provide key information for understanding its origin. Figure 3a shows a detailed band structure measured at 0.9 K along a momentum cut that is nearly parallel to the Γ–M direction. To directly visualize the gap opening and remove the effect of the Fermi cutoff, the image was obtained by symmetrizing the original data with respect to the Fermi level. The corresponding EDCs and symmetrized EDCs are shown in Fig. 3c,d, respectively. The band structure of ε′ in the superconducting state, E_k, was directly extracted from the symmetrized EDCs (Fig. 3d) and plotted in Fig. 3e as pink circles. The superconducting gap was also determined directly from the symmetrized EDCs (Fig. 3d) which are 0.8 meV and 0 meV for the left and right Fermi momenta of the ε′ band ($k_F^{\varepsilon'_L}$ and $k_F^{\varepsilon'_R}$), respectively. Assuming a linear variation of the superconducting gap between the two Fermi momenta (Δ_k), we obtained the normal state ε′ band structure (e_k) by using the BCS (Bardeen–Cooper–Schrieffer theory) relationship $E_k^2 = e_k^2 + \Delta_k^2$, as shown by the blue line in Fig. 3e. The normal state ε′ band was strikingly flat and its band top was only about 1 meV above the Fermi level. The effective masses obtained from the left side and the right side of the ε′ band were $3.2m_e$ and $13.8m_e$, respectively, where m_e is the mass of a free electron. Such a dramatic anisotropy of the effective mass is understandable because the two sides of the ε′ band come from

https://doi.org/10.1038/s41567-023-02348-1

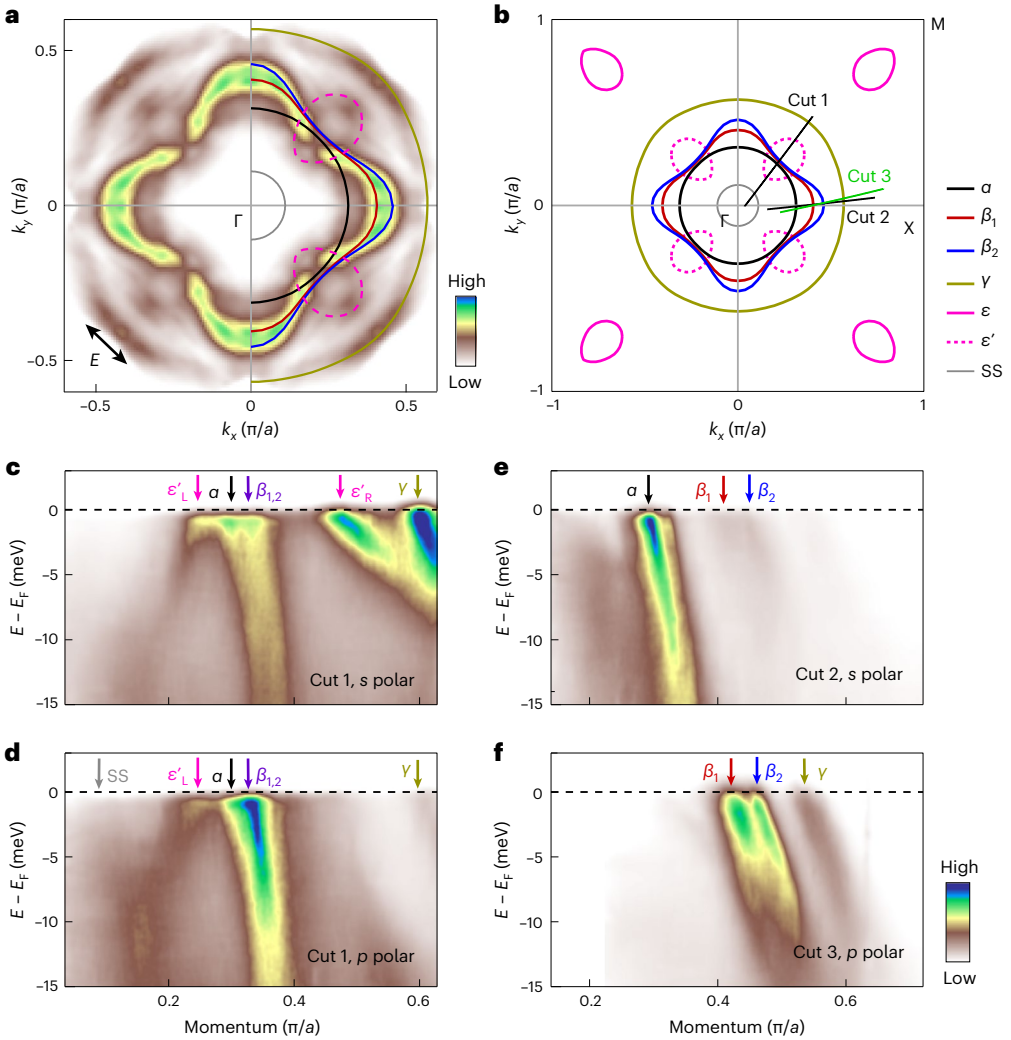

Fig. 1 | Fermi surface and band structures of KFe_2As_2 measured at 0.9 K. **a**, Fermi surface mapping near the zone centre Γ point. It is obtained by integrating the spectral intensity within ±1 meV with respect to the Fermi level and is symmetrized assuming fourfold symmetry. **b**, Measured Fermi surface obtained by analysing the Fermi surface mappings and band structures measured under different polarization geometries (Supplementary Fig. 2). The four ε′ pockets around Γ are produced by folding of the four ε pockets around M due to $\sqrt{2} \times \sqrt{2}$ surface reconstruction. **c**–**f**, Typical band structures measured along Cut1 via *s* polarization, Cut1 via *p* polarization, Cut2 via *s* polarization and Cut3 via *p* polarization, respectively. The location of the momentum cuts is marked in **b** while the *s* and *p* polariation are defined in Supplementary Fig. 2. The observed bands are marked by arrows of different colours.

different orbitals, as seen in Fig. 3f. In particular, when compared with the band structure calculations (Fig. 3f)[35], the effective masses for the left side and the right side of the ε band reached $16m_b$ and $8.1m_b$, where m_b is the corresponding band mass. The Fermi energy of the ε band shrank strongly from the calculated 20 meV to the measured 1 meV. Such a huge band renormalization of the ε band is among the strongest observed in iron-based superconductors[44].

Our detailed band structure measurements indicate that the large specific heat and the associated heavy Fermion behaviours discovered in KFe_2As_2 (refs. 33,35–40) originate from strong band renormalizations, in particular, of the ε band. Similarly to the ε′ band in Fig. 3e,f, we carried out band structure analysis of the α, β and γ bands along different directions (Supplementary Fig. 11) to extract the effective mass (m^*) and the Sommerfeld coefficient γ, as shown in Supplementary Fig. 11e,f and listed in Supplementary Table 3. All the bands exhibited strongly enhanced effective mass, with the γ band reaching more than 20 times the value of m_e (Supplementary Fig. 11e and Supplementary Table 3). When compared with the calculated band structures, the ε band showed the strongest renormalization with m^*/m_b greater than 15 (Supplementary Fig. 11f and Supplementary Table 3). The anomalously large specific heat found in KFe_2As_2 comes from the combined contributions of all of these renormalized bands. In spite of its small Fermi surface area, the ε band plays a considerable role in contributing to the specific heat; nearly half of the Sommerfeld coefficient is contributed by the ε band (Supplementary Table 3).

Now, we come to the determination of the superconducting gap in KFe_2As_2. Because KFe_2As_2 is a typical multiorbital system and strong matrix element effects are involved in the ARPES measurements (Fig. 1), to extract the superconducting gap along all the Fermi surface sheets, we carried out ARPES measurements along different momentum cuts under different polarization geometries, and we repeated the measurements on many KFe_2As_2 samples (Supplementary Figs. 12–17 for the α, β, γ, ε′ and SS, respectively). Figure 4a–e shows the symmetrized EDCs along the α, β_1, β_2, γ and ε′ Fermi surface sheets. The gap size was determined by the peak position in the symmetrized EDCs[43] (for detailed discussion of the gap determination, see Supplementary Figs. 18–20). The measured superconducting gap along the α, β_1, β_2 and γ Fermi surfaces is presented in Fig. 4f and the gap along the ε Fermi surface is shown in Fig. 4g. The superconducting gap along the ε Fermi surface was not measured in the previous ARPES measurement[21],

https://doi.org/10.1038/s41567-023-02348-1

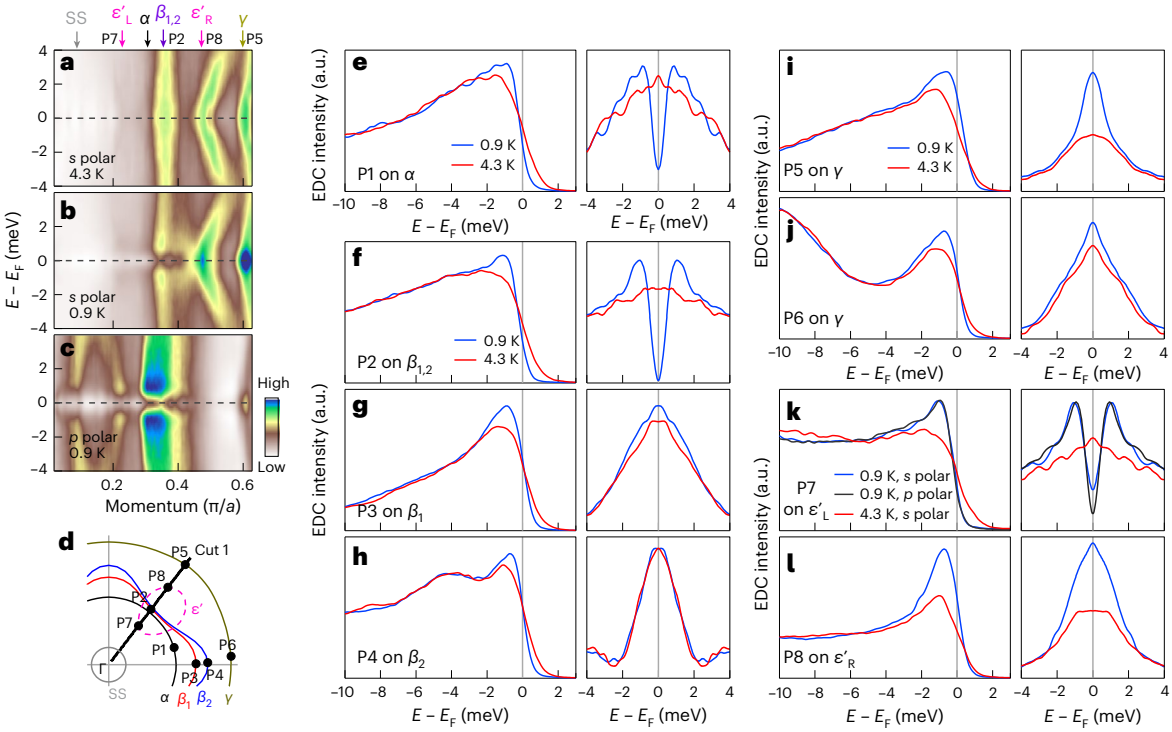

Fig. 2 | Superconducting gap opening along different Fermi surface sheets by measuring photoemission spectra in the normal and superconducting states. a–c, Band structures measured along the same momentum cut at different temperatures under different polarization geometries. The location of the momentum cut (Cut 1) is marked by the black line in **d**. **a**, Band structures were measured in the normal state at 4.3 K under the *s* polarization. **b**, The same as **a** but measured at 0.9 K in the superconducting state. **c**, The same as **b** but measured under the *p* polarization. To directly visualize the gap opening, these images were obtained by symmetrizing the original data with respect to the Fermi level. **d**, Fermi surface of KFe_2As_2 marked with the momentum cut used in **a**–**c** and the Fermi momentum points P1–P8 used in **e**–**l**. **e**, EDCs (left panel) and the corresponding symmetrized EDCs (right panel) measured at the Fermi momentum P1 along the α Fermi surface in the normal (4.3 K) and superconducting (0.9 K) states. The location of the P1 point is marked in **d**. **f**–**h**, Same as **e** but measured at the Fermi momenta P2 (**f**), P3 (**g**) and P4 (**h**) along the β Fermi surface sheets (β_1 and β_2). **i**–**j**, Same as **e** but measured at the Fermi momenta P5 (**i**) and P6 (**j**) along the γ Fermi surface sheet. **k**–**l**, Same as **e** but measured at the Fermi momenta P7 (**k**) and P8 (**l**) along the ε' Fermi surface sheet. To facilitate a comparison, in **k**, the two EDCs measured at 0.9 K under *s* and *p* polarizations were normalized in intensity near the Fermi level.

however, it has been measured here. Figure 4i shows a three-dimensional plot of the measured superconducting gap structure in KFe_2As_2. As seen in Fig. 4f, the α Fermi surface shows a large superconducting gap (nearly 1.0 meV) that is nearly isotropic, with a small variation of ±0.1 meV. The superconducting gap of the β Fermi surface (β_1 and β_2) is highly anisotropic. It is nearly zero along the Γ–X direction and reaches a maximum (nearly 1.0 meV) along the Γ–M direction. Along the entire γ Fermi surface, the gap is nearly zero within our detection limit. We note that our results of the superconducting gap along the α, β and γ Fermi surfaces around Γ (Fig. 4f) are notably different from those reported before[21] (the reason for the discrepancy is discussed in the Supplementary Information). As seen in Fig. 4g, the superconducting gap on the small ε pocket is highly anisotropic. Along the Γ–M direction, it is maximum near the tip close to M whereas it approaches zero on the other side away from M. The superconducting gap structure in KFe_2As_2 is quite distinct along different Fermi surface sheets.

Our precise determination of the electronic structure and superconducting gap structure, in particular, for the ε Fermi surface around M, provides a correct picture of the pairing symmetry in KFe_2As_2. Based on the following observations, we find that our results are consistent with $s_\pm$ pairing symmetry with sign reversal between the Γ and M points. First, the superconducting gap size along all the Fermi surface sheets is qualitatively consistent with the simple $s_\pm$ form: $|\Delta| = \Delta_0|\cos k_x + \cos k_y|$, as shown in Fig. 5a. In the $s_\pm$ pairing symmetry with the simplest form, the gap size is expected to decrease with increasing distance of the momentum point from Γ or M (thick black line and thick red line in Fig. 5a). The measured superconducting gap of KFe_2As_2, extracted from many data points on different Fermi surface sheets, is found to also decrease with increasing distance of the momentum point from Γ or M (data points in Fig. 5a). Second, precise nesting vectors along Γ–M can be determined from our measured Fermi surface (Fig. 5b). They are consistent with the previous ARPES measurements[34] and show rather weak k_z dependence[34]. If the nestings connect the α and β Fermi surface around Γ, as previously proposed[27,31], the corresponding nesting vectors obtained from Fig. 5b are 0.61π/a and 2.21π/a (a, lattice constant) along the Γ–M direction, which significantly deviate from the two spin resonance wavevectors of 0.85π/a and 1.98π/a from neutron scattering measurements[31] (Supplementary Fig. 21). On the other hand, when the two vectors connect the best nested portion of the ε Fermi surface around M and the α or β Fermi surface around Γ, as identified in Fig. 5b, the obtained wavevectors of $\mathbf{Q}_1 = 0.87\pi/a$ and $\mathbf{Q}_2 = 1.96\pi/a$ have a perfect match to the two spin resonance wavevectors[31]. This indicates that the two regions connected by the nesting vectors have the reversed sign of the superconducting gap. This is consistent with the $s_\pm$ form $\Delta = \Delta_0(\cos k_x + \cos k_y)$, as depicted in Fig. 5b. Neutron scattering measurements found that the spin resonance peak in $(Ba_{1-x}K_x)Fe_2As_2$ gets weaker as doping is increased in the overdoped region due to the increasing mismatch between the hole pocket around Γ and the electron pocket around M (refs. 45,46). In KFe_2As_2 where the ε hole pockets emerge around M, the spin resonance peak is observed but is much weaker than that in optimally doped $(Ba_{0.6}K_{0.4})Fe_2As_2$ (ref. 31). This is consistent with the Fermi surface nesting but with a relatively small nested area in KFe_2As_2. Third, the nesting vectors connect portions of the two Fermi surface that have the maximum superconducting gap (black solid circles in Fig. 5b). It has been found that the energy of the resonance mode E_R and the superconducting gap Δ_{tot} follow the

https://doi.org/10.1038/s41567-023-02348-1

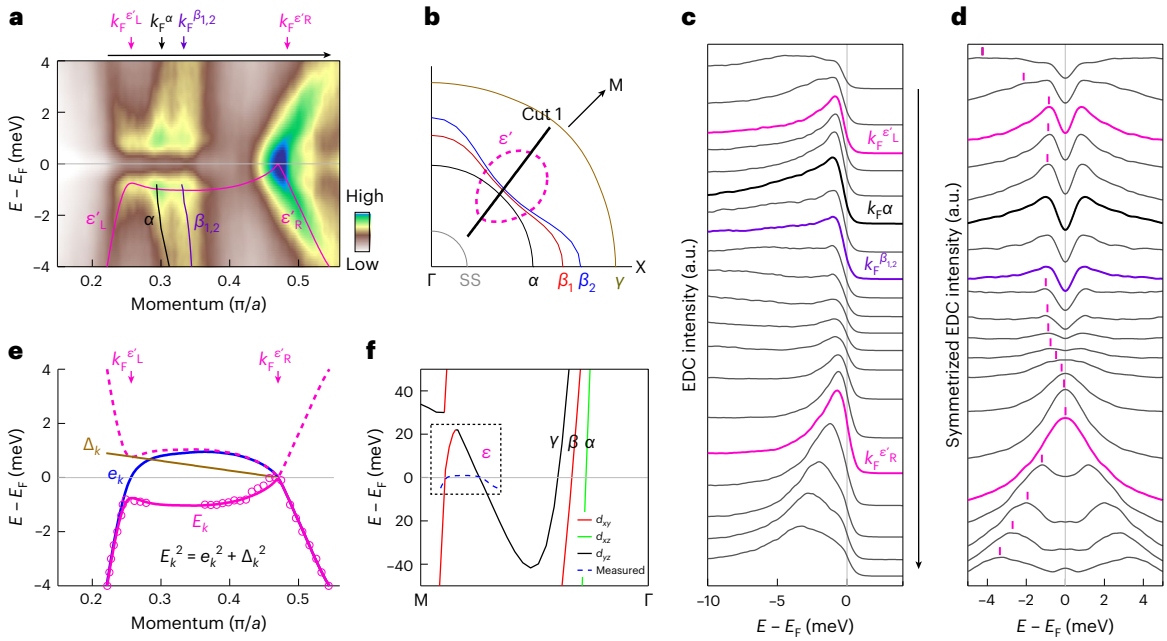

Fig. 3 | Detailed analysis of the ε band in the superconducting state. a, Band structure measured along a momentum cut that is nearly parallel to the Γ–M direction. The location of the momentum cut (Cut 1) is marked by the black line in **b**. The image was obtained by symmetrizing the original data with respect to the Fermi level. The observed bands, α, $\beta_{1,2}$ and ε', are marked by black, purple and pink lines, respectively. **b**, Fermi surface of KFe_2As_2 marked with the momentum cut (Cut 1) used in **a**. **c**, Original EDCs from the original data in **a** before symmetrization in the momentum range marked by the black line with an arrow on top of **a**. The EDCs at the Fermi momenta of the α, $\beta_{1,2}$ and ε' bands are marked by colours. **d**, The corresponding symmetrized EDCs obtained from **c**. The EDC peaks corresponding to the ε' band and its Bogoliubov band are marked by pink ticks. **e**, Quantitative determination of the ε' band dispersion (pink circles) in the superconducting state from **a** and **d**, which is described by continuous pink lines (E_k). Since the gap size is zero at the right Fermi momentum ($k_F^{\varepsilon' R}$) and 0.8 meV at the left Fermi momentum ($k_F^{\varepsilon' L}$), a linear variation of the gap, Δ_k, between the Fermi momenta is assumed (brown line). The dispersion in the normal state ε_k (blue curve) was then derived using the equation $E_k^2 = e_k^2 + \Delta_k^2$ from BCS theory. **f**, The calculated band structure shows where the measured ε band is located using a black dashed frame. The measured ε band is also plotted (blue dashed line) for a direct comparison.

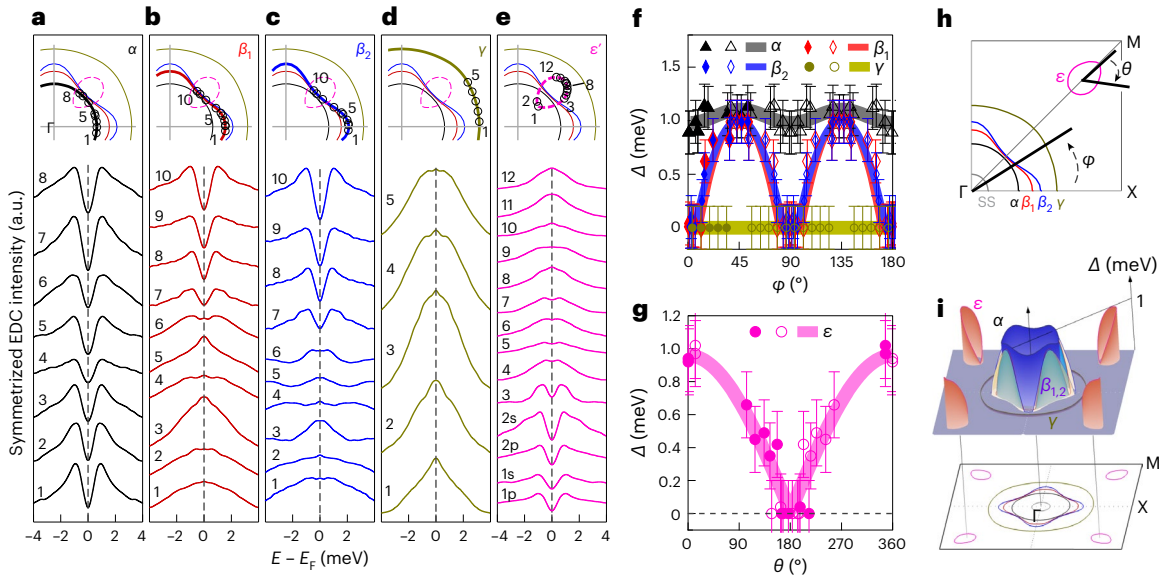

Fig. 4 | Momentum-dependent superconducting gaps along all the Fermi surface sheets of KFe_2As_2. a–**e**, Symmetrized EDCs along the α (**a**), β_1 (**b**), β_2 (**c**), γ (**d**) and ε' (**e**) Fermi surface sheets, respectively. The Fermi momentum positions are marked by empty circles in the inset Fermi surface. The details of extracting these symmetrized EDCs are described in Supplementary Figs. 13–17. **f**–**h**, The momentum-dependent superconducting gap as a function of the Fermi surface angle φ for the α, β_1, β_2 and γ Fermi surfaces (**f**) and as a function of θ for the ε Fermi surface (**g**). The Fermi surface angles φ and θ are defined in **h**. The solid symbols were derived from the symmetrized EDCs shown in **a**–**e** whereas the open symbols were obtained by symmetrization, taking into account the fourfold symmetry. The uncertainties are marked by error bars. The thick lines are the fitted curves of the measured gaps. **i**, Three-dimensional plot of the superconducting gaps in KFe_2As_2. The corresponding Fermi surface is shown at the bottom.

https://doi.org/10.1038/s41567-023-02348-1

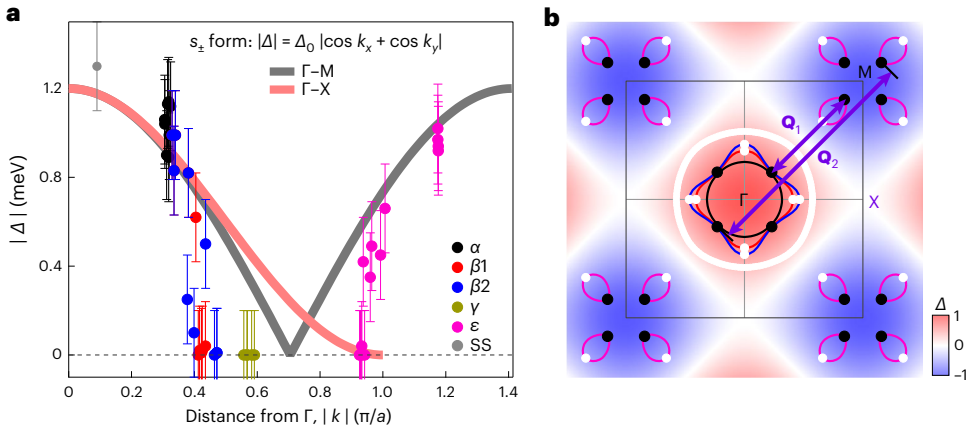

Fig. 5 | Gap symmetry of KFe_2As_2. a, The superconducting gap as a function of the distance between the Fermi momentum and the Γ point on all the Fermi surface sheets. The uncertainties are marked by error bars. The expected gap size variation from the $s_\pm$ symmetry with the gap form $|\cos k_x + \cos k_y|$ (ref. 55) is plotted as a thick black line along the Γ–M direction and as a thick red line along the Γ–X direction. **b**, Gap nodes and local gap maxima on the Fermi surface of KFe_2As_2. The Fermi surfaces are plotted on top of a two-dimensional image showing the gap function $\cos k_x + \cos k_y$ in the $s_\pm$ pairing symmetry, where the positive gap sign, negative gap sign and the gap nodes are represented by red, blue and white colours, respectively. The measured gap nodes are marked by white circles and the gap maxima are marked by black circles. Two interband scattering wavevectors ($\mathbf{Q}_1$ and $\mathbf{Q}_2$) are marked by double-arrow purple lines. $\mathbf{Q}_1$ and $\mathbf{Q}_2$ connect the local gap maxima between the ε band and the (α, β) bands.

universal relationship $E_R/\Delta_{tot} \approx 0.64$ in iron-based superconductors, where Δ_{tot} is the total superconducting gap summed on the two Fermi surfaces linked by the nesting vectors[47]. The total gap size $\Delta_{tot} = 2.0$ meV, where 1.0 meV is from the α or β Fermi surface and the other 1.0 meV is from the ε Fermi surface. The energy of the resonance mode in KFe_2As_2 was then estimated to be 1.28 meV, which is in a good agreement with that measured in neutron scattering (1.2 meV) (ref. 31). Fourth, from the measured superconducting gap structure, we identified the nearly zero gap points on the β, γ and ε Fermi surfaces, as marked by the white circles in Fig. 5b. In the $s_\pm$ gap symmetry, there were zero gap nodal regions along the $(0, \pm\pi)$–$(\pm\pi, 0)$ lines (Fig. 5b). It is interesting to note that the measured momentum region with nearly zero gap on the β and ε Fermi surfaces was located closest to the zero gap lines of the $s_\pm$ form. In particular, the γ Fermi surface lay very close to the $s_\pm$ nodal lines and the superconducting gap was nearly zero along the entire Fermi surface. These results indicate that sign reversal $s_\pm$ pairing symmetry can be realized in a system with only hole pockets. Here the sign change occurs between the hole pockets around Γ and those around M. Previously, the $s_\pm$ pairing symmetry was proposed and tested in superconductors with hole pockets around Γ and electron pockets around M (refs. 5,6,8,48,49). Neutron scatterings have observed spin fluctuations in KFe_2As_2 (refs. 31,50,51) and spin fluctuation exchange always leads to a repulsive interaction and can only realize sign-changing superconducting states[1]. Therefore, our identification of the nodal $s_\pm$ pairing symmetry in KFe_2As_2 indicates that the spin fluctuations may play a dominant role in generating superconductivity even in a system with only hole pockets.

The determination of the pairing symmetry is essential for understanding the superconductivity mechanism of iron-based superconductors. Our present work has substantial implications for the pairing symmetry in KFe_2As_2. The pairing symmetry in heavily hole-doped iron-based superconductors with only hole pockets has been extensively studied theoretically and experimentally. Various possibilities have been proposed and debated, including the competition of $s_\pm$ (Γ–M) and d (ref. 28), pure extended d (refs. 26,52), pure $s_\pm$ (Γ–M) (ref. 53), the competition between $s_\pm$ (two hole pockets around Γ) and d (ref. 54) and pure $s_\pm$ (two hole pockets around the zone centre)[27]. In particular, based on the previous ARPES results on the superconducting gap of KFe_2As_2 (ref. 21), the focus has been on pure $s_\pm$ with sign reversal between the two hole pockets (h_1 and h_2) around the zone centre[27]. The neutron scattering measurements on KFe_2As_2 are considered to be consistent with this $s_\pm$ (h_1–h_2) symmetry[31]. Our present results have corrected the previous ARPES results[21], pinned down on a different pairing picture in KFe_2As_2, and have provided key information for theoretically understanding the pairing symmetry in iron-based superconductors with only hole pockets. Furthermore, our results have provided a unified picture of the pairing symmetry in iron-based superconductors with distinct Fermi surface topologies. As a typical multiband system, the pairing symmetry in iron-based superconductors is usually considered to be closely related to the Fermi surface topology. When there are both hole-like Fermi surfaces around Γ and electron-like Fermi surfaces around M, the pairing symmetry is generally believed to be $s_\pm$, with the sign change occurring between Γ and M (refs. 1–8,49). When there are only hole pockets in heavily hole-doped iron-based superconductors, the pairing symmetry is highly controversial[26–28,52,53] and a pairing symmetry transition is proposed with increasing hole doping[26,30,52,54]. Our finding of a common $s_\pm$ (Γ–M) pairing symmetry indicates that the system with both the electron and hole pockets and the system with only hole pockets may share a similar pairing mechanism that can be described by a unified theoretical framework.

Online content

Any methods, additional references, Nature Portfolio reporting summaries, source data, extended data, supplementary information, acknowledgements, peer review information; details of author contributions and competing interests; and statements of data and code availability are available at https://doi.org/10.1038/s41567-023-02348-1.

References

1. Hirschfeld, P. J., Korshunov, M. M. & Mazin, I. I. Gap symmetry and structure of Fe-based superconductors. *Rep. Prog. Phys.* **74**, 124508 (2011).
2. Wang, F. & Lee, D. H. The electron-pairing mechanism of iron-based superconductors. *Science* **332**, 200–204 (2011).
3. Hosono, H. & Kuroki, K. Iron-based superconductors: current status of materials and pairing mechanism. *Phys. C.* **514**, 399–422 (2015).
4. Fernandes, R. M. et al. Iron pnictides and chalcogenides: a new paradigm for superconductivity. *Nature* **601**, 35–44 (2022).
5. Mazin, I. I., Singh, D. J., Johannes, M. D. & Du, M. H. Unconventional superconductivity with a sign reversal in the order parameter of $LaFeAsO_{1-x}F_x$. *Phys. Rev. Lett.* **101**, 057003 (2008).

6. Kuroki, K. et al. Unconventional pairing originating from the disconnected Fermi surfaces of superconducting $LaFeAsO_{1-x}F_x$. *Phys. Rev. Lett.* **101**, 087004 (2008).
7. Si, Q. & Abrahams, E. Strong correlations and magnetic frustration in the high T_c iron pnictides. *Phys. Rev. Lett.* **101**, 076401 (2008).
8. Seo, K., Bernevig, B. A. & Hu, J. Pairing symmetry in a two-orbital exchange coupling model of oxypnictides. *Phys. Rev. Lett.* **101**, 206404 (2008).
9. Zhang, Y. et al. Nodeless superconducting gap in $A_xFe_2Se_2$ (A=K,Cs) revealed by angle-resolved photoemission spectroscopy. *Nat. Mater.* **10**, 273–277 (2011).
10. Qian, T. et al. Absence of a holelike Fermi surface for the iron-based $K_{0.8}F_{1.7}Se_2$ superconductor revealed by angle-resolved photoemission spectroscopy. *Phys. Rev. Lett.* **106**, 187001 (2011).
11. Mou, D. et al. Distinct Fermi surface topology and nodeless superconducting gap in a $(Tl_{0.58}Rb_{0.42})Fe_{1.72}Se_2$ superconductor. *Phys. Rev. Lett.* **106**, 107001 (2011).
12. Liu, D. et al. Electronic origin of high-temperature superconductivity in single-layer FeSe superconductor. *Nat. Commun.* **3**, 931 (2012).
13. Zhao, L. et al. Common electronic origin of superconductivity in (Li,Fe)OHFeSe bulk superconductor and single-layer FeSe/$SrTiO_3$ films. *Nat. Commun.* **7**, 10608 (2016).
14. Maier, T. A., Graser, S., Hirschfeld, P. J. & Scalapino, D. J. *d*-wave pairing from spin fluctuations in the $K_xFe_{2-y}Se_2$ superconductors. *Phys. Rev. B* **83**, 100515 (2011).
15. Wang, F. et al. The electron pairing of $K_xFe_{2-y}Se_2$. *Europhys. Lett.* **93**, 57003 (2011).
16. Khodas, M. & Chubukov, A. V. Interpocket pairing and gap symmetry in Fe-based superconductors with only electron pockets. *Phys. Rev. Lett.* **108**, 247003 (2012).
17. Fukazawa, H. et al. Possible multiple gap superconductivity with line nodes in heavily hole-doped superconductor KFe_2As_2 studied by ^{75}As nuclear quadrupole resonance and specific heat. *J. Phys. Soc. Japan* **78**, 083712 (2009).
18. Dong, J. K. et al. Quantum criticality and nodal superconductivity in the FeAs-based superconductor KFe_2As_2. *Phys. Rev. Lett.* **104**, 087005 (2010).
19. Hashimoto, K. et al. Evidence for superconducting gap nodes in the zone-centered hole bands of KFe_2As_2 from magnetic penetration-depth measurements. *Phys. Rev. B* **82**, 014526 (2010).
20. Reid, J. P. et al. Universal heat conduction in the iron arsenide superconductor KFe_2As_2: evidence of a *d*-wave state. *Phys. Rev. Lett.* **109**, 087001 (2012).
21. Okazaki, K. et al. Octet-line node structure of superconducting order parameter in KFe_2As_2. *Science* **337**, 1314–1317 (2012).
22. Xu, N. et al. Possible nodal superconducting gap and Lifshitz transition in heavily hole-doped $Ba_{0.1}K_{0.9}Fe_2As_2$. *Phys. Rev. B* **88**, 220508 (2013).
23. Watanabe, D. et al. Doping evolution of the quasiparticle excitations in heavily hole-doped $Ba_{1-x}K_xFe_2As_2$: a possible superconducting gap with sign-reversal between hole pockets. *Phys. Rev. B* **89**, 115112 (2014).
24. Kyuil, C. et al. Energy gap evolution across the superconductivity dome in single crystals of $(Ba_{1-x}K_x)Fe_2As_2$. *Sci. Adv.* **2**, e1600807 (2016).
25. Hardy, F. et al. Strong correlations, strong coupling, and *s*-wave superconductivity in hole-doped $BaFe_2As_2$ single crystals. *Phys. Rev. B* **94**, 205113 (2016).
26. Thomale, R., Platt, C., Hanke, W., Hu, J. & Bernevig, B. A. Exotic *d*-wave superconducting state of strongly hole-doped $K_xBa_{1-x}Fe_2As_2$. *Phys. Rev. Lett.* **107**, 117001 (2011).
27. Maiti, S., Korshunov, M. M. & Chubukov, A. V. Gap symmetry in KFe_2As_2 and the $\cos 4\theta$ gap component in LiFeAs. *Phys. Rev. B* **85**, 014511 (2012).
28. Suzuki, K., Usui, H. & Kuroki, K. Spin fluctuations and unconventional pairing in KFe_2As_2. *Phys. Rev. B* **84**, 144514 (2011).
29. Tafti, F. F. et al. Sudden reversal in the pressure dependence of T_c in the iron-based superconductor KFe_2As_2. *Nat. Phys.* **9**, 349–352 (2013).
30. Grinenko, V. et al. Superconductivity with broken time-reversal symmetry inside a superconducting *s*-wave state. *Nat. Phys.* **16**, 789–794 (2020).
31. Shen, S. et al. Neutron spin resonance in the heavily hole-doped KFe_2As_2 superconductor. *Phys. Rev. Lett.* **124**, 017001 (2020).
32. Sato, T. et al. Band structure and Fermi surface of an extremely overdoped iron-based superconductor KFe_2As_2. *Phys. Rev. Lett.* **103**, 047002 (2009).
33. Terashima, T. et al. Fermi surface in KFe_2As_2 determined via de Haas-van Alphen oscillation measurements. *Phys. Rev. B* **87**, 224512 (2013).
34. Yoshida, T. et al. Orbital character and electron correlation effects on two- and three-dimensional Fermi surfaces in KFe_2As_2 revealed by angle-resolved photoemission spectroscopy. *Front. Phys.* **2**, 17 (2014).
35. Terashima, T. et al. Fermi surface and mass enhancement in KFe_2As_2 from de Haas-van Alphen effect measurements. *J. Phys. Soc. Japan* **79**, 053702 (2010).
36. Kim, J. S., Kim, E. G., Stewart, G. R., Chen, X. H. & Wang, X. F. Specific heat in KFe_2As_2 in zero and applied magnetic field. *Phys. Rev. B* **83**, 172502 (2011).
37. Abdel-Hafiez, M. et al. Specific heat and upper critical fields in KFe_2As_2 single crystals. *Phys. Rev. B* **85**, 134533 (2012).
38. Hardy, F. et al. Evidence of strong correlations and coherence-incoherence crossover in the iron pnictide superconductor KFe_2As_2. *Phys. Rev. Lett.* **111**, 027002 (2013).
39. Eilers, F. et al. Strain-driven approach to quantum criticality in AFe_2As_2 with A=K, Rb, and Cs. *Phys. Rev. Lett.* **116**, 237003 (2016).
40. Wu, Y. P. et al. Emergent Kondo lattice behavior in iron-based superconductors AFe_2As_2 (A=K, Rb, Cs). *Phys. Rev. Lett.* **116**, 147001 (2016).
41. de' Medici, L., Giovannetti, G. & Capone, M. Selective Mott physics as a key to iron superconductors. *Phys. Rev. Lett.* **112**, 177001 (2014).
42. Zhou, X. et al. New developments in laser-based photoemission spectroscopy and its scientific applications: a key issues review. *Rep. Prog. Phys.* **81**, 062101 (2018).
43. Norman, M. R., Randeria, M., Ding, H. & Campuzano, J. C. Phenomenology of the low-energy spectral function in high-*Tc* superconductors. *Phys. Rev. B* **57**, 4 (1998).
44. Tamai, A. et al. Strong electron correlations in the normal state of the iron-based $FeSe_{0.42}Te_{0.58}$ superconductor observed by angle-resolved photoemission spectroscopy. *Phys. Rev. Lett.* **104**, 097002 (2010).
45. Castellan, J. P. et al. Effect of Fermi surface nesting on resonant spin excitations in $Ba_{1-x}K_xFe_2As_2$. *Phys. Rev. Lett.* **107**, 177003 (2011).
46. Lee, C. H. et al. Suppression of spin-exciton state in hole overdoped iron-based superconductors. *Sci. Rep.* **6**, 23424 (2016).
47. Yu, G., Li, Y., Motoyama, E. M. & Greven, M. A universal relationship between magnetic resonance and superconducting gap in unconventional superconductors. *Nat. Phys.* **5**, 873–875 (2009).
48. Wang, F., Zhai, H., Ran, Y., Vishwanath, A. & Lee, D. H. Functional renormalization-group study of the pairing symmetry and pairing mechanism of the FeAs-based high-temperature superconductor. *Phys. Rev. Lett.* **102**, 047005 (2009).

49. Hanaguri, T., Niitaka, S., Kuroki, K. & Takagi, H. Unconventional s-wave superconductivity in Fe(Se,Te). *Science* **328**, 474–476 (2010).
50. Lee, C. H. et al. Incommensurate spin fluctuations in hole-overdoped superconductor KFe_2As_2. *Phys. Rev. Lett.* **106**, 067003 (2011).
51. Horigane, K. et al. Spin excitations in hole-overdoped iron-based superconductors. *Sci. Rep.* **6**, 33303 (2016).
52. Platt, C., Li, G., Fink, M., Hanke, W. & Thomale, R. Evolution of superconducting gap anisotropy in hole-doped 122 iron pnictides. *Phys. Status Solidi B* **254**, 1600350 (2017).
53. Bang, Y. A shadow gap in the over-doped $(Ba_{1-x}K_x)Fe_2As_2$ compound. *New J. Phys.* **16**, 023029 (2014).
54. Maiti, S., Korshunov, M. M., Maier, T. A., Hirschfeld, P. J. & Chubukov, A. V. Evolution of the superconducting state of Fe-based compounds with doping. *Phys. Rev. Lett.* **107**, 147002 (2011).
55. Hu, J. & Ding, H. Local antiferromagnetic exchange and collaborative fermi surface as key ingredients of high temperature superconductors. *Sci. Rep.* **2**, 381 (2012).

Methods

High-quality single crystals of KFe_2As_2 were grown by the KAs flux method[56]. The samples were characterized by magnetic susceptibility measurements (Supplementary Fig. 1a) and the measured T_C was 3.7 K with a narrow transition width of 0.2 K. The residual resistivity rate ($R_{300\,K}/R_{0\,K}$) of near 1,000 was obtained from the resistivity measurement (Supplementary Fig. 1b). Both measurements indicated that our KFe_2As_2 single crystal samples were of very high quality.

High-resolution angle-resolved photoemission measurements were carried out by using our laboratory-based ARPES system. It was equipped with a vacuum-ultraviolet laser with a photon energy of $h\nu$ = 6.994 eV and a hemispherical electron energy analyser R8000 (Scienta-Omicron). The light polarization could be varied to get linear polarization along different directions and circular polarization. This system used ^{3}He pumping technology which could cool the sample down to the lowest temperature of 0.8 K. The energy resolution was set at 0.5 meV and the angular resolution was 0.3°, corresponding to 0.004 $Å^{-1}$ momentum resolution at the photon energy of 6.994 eV. All the samples were cleaved in situ at low temperature and measured in an ultrahigh vacuum with a base pressure better than 1×10^{-10} mbar. The Fermi level was carefully referenced by measuring polycrystalline gold which was well connected with the sample.

The photon-energy-dependent ARPES measurements were performed at the Bloch beamline of MAX IV, equipped with a hemispherical electron energy analyser DA30-L (Scienta-Omicron). The angular resolution was ≤0.2° and the overall energy resolution was ≤10 meV. The single crystals were cleaved in situ at low temperature and measured in an ultrahigh vacuum with a base pressure better than 1×10^{-10} mbar.

Data availability

All raw data generated during the study are available from the corresponding authors upon request. Source data are provided with this paper.

Code availability

The codes used for the fitting and simulation process in this study are available from the corresponding authors upon request.

References

56. Kihou, K. et al. Single-crystal growth of $Ba_{1-x}K_xFe_2As_2$ by KAs self-flux method. *J. Phys. Soc. Japan* **85**, 034718 (2016).

Acknowledgements

This work is supported by: the National Key Research and Development Program of China (grant nos. 2021YFA1401800 (to X.J.Z.), 2017YFA0302900 (to H.Q.M.), 2018YFA0704200 (to H.Q.M.), 2018YFA0305600 (to G.D.L.), 2019YFA0308000 (to H.Q.M.) and 2022YFA1604203 (to L.Z.)); the National Natural Science Foundation of China (grant nos. 11888101 (to X.J.Z.), 11922414 (to L.Z.) and 11974404 (to G.D.L.)); the Strategic Priority Research Program (B) of the Chinese Academy of Sciences (grant nos. XDB25000000 (to X.J.Z.) and XDB33000000 (to H.Q.M.)); the Innovation Program for Quantum Science and Technology (grant no. 2021ZD0301800 (to X.J.Z.)); the Youth Innovation Promotion Association of CAS (grant nos. Y2021006 (to L.Z.) and Y202001 (to H.Q.L.)); and the Synergetic Extreme Condition User Facility (SECUF) (to X.J.Z.). We thank the MAX IV Laboratory for time on Beamline Bloch under Proposal 20221180. Research conducted at MAX IV, a Swedish national user facility, was supported by the Swedish Research council under contract 2018-07152, the Swedish Governmental Agency for Innovation Systems under contract 2018-04969 and Formas under contract 2019-02496. We thank C. Polley and B. Thiagarajan at Beamline Bloch of MAX IV for supporting the beamtime.

Author contributions

X.J.Z., L.Z. and D.S.W. proposed and designed the research. D.S.W., W.S.H., Y.J.S., H.Q.L. and S.L.L. contributed to the sample growth and the magnetic and resistivity measurements. J.J.J., J.G.Y., H.T.Y., H.T.R., P.A., X.Z., C.H.Y., T.M.M., C.L.L., S.J.Z., F.F.Z., F.Y., Z.M.W., N.Z., L.J.L., R.K.L., X.Y.W., Q.J.P., H.Q.M., G.D.L., Z.Y.X., L.Z. and X.J.Z. contributed to the development and maintenance of the ARPES systems and related software development. D.S.W. carried out the ARPES experiment with J.J.J., J.G.Y., J.Y.L., H.K.C., Y.H.Y., C.P., Y.L.C., L.Z. and X.J.Z. D.S.W., L.Z. and X.J.Z. analysed the data. X.X.W. contributed to the band structure calculations. X.J.Z., L.Z. and D.S.W. wrote the paper. All authors participated in discussion and commented on the paper.

Competing interests

The authors declare no competing interests.

Additional information

Supplementary information The online version contains supplementary material available at https://doi.org/10.1038/s41567-023-02348-1.

Correspondence and requests for materials should be addressed to Lin Zhao or X. J. Zhou.

Peer review information *Nature Physics* thanks the anonymous reviewers for their contribution to the peer review of this work.